Lattice stress states of superhard tungsten tetraboride from radial x-ray diffraction under nonhydrostatic compression

Miao Xie, Reza Mohammadi, Christopher L. Turner, Richard B. Kaner, Abby Kavner, and Sarah H. Tolbert

Phys. Rev. B **90**, 104104 — Published 8 September 2014

DOI: 10.1103/PhysRevB.90.104104

Lattice Stress States of Superhard Tungsten Tetraboride from Radial X-ray Diffraction under Non-hydrostatic Compression

Miao Xie,[1] Reza Mohammadi,[1,2†] Christopher L. Turner,[1] Richard B. Kaner,[1,2,3,*] Abby Kavner,[4,*] and Sarah H. Tolbert[1,2,3,*]

[1]*Department of Chemistry and Biochemistry, University of California, Los Angeles, CA, USA*

[2]*Department of Materials Science and Engineering, University of California, Los Angeles, CA, USA*

[3]*California NanoSystems Institute (CNSI), University of California, Los Angeles, CA, USA*

[4]*Department of Earth and Space Sciences, University of California, Los Angeles, CA, USA*

*Corresponding authors. tolbert@chem.ucla.edu, akavner@ucla.edu, kaner@chem.ucla.edu

[†]Current address: Department of Mechanical and Nuclear Engineering, School of Engineering, Virginia Commonwealth University, Richmond, VA 23284-3067

ABSTRACT

In this work, we examine the lattice behavior of the economically interesting superhard material, tungsten tetraboride (WB_4), in a diamond anvil cell under non-hydrostatic compression up to 48.5 GPa. From the measurements of lattice-supported differential stress, significant strength anisotropy is observed in WB_4. The (002) planes are found to support the highest differential stress of 19.7 GPa within the applied pressure range. This result is in contrast to ReB_2, one of the hardest transition metal borides known to date, where the same planes support the least differential stress. A discontinuous change in the slope of *c/a* ratio is seen at 15 GPa, suggesting a structural phase transition that has also been observed under hydrostatic compression. Speculations on the possible relationship between the observed structural changes, the strength anisotropy, and the orientation of boron-boron bonds along the *c* direction within the WB_4 structure are included.

Keywords: Axial diffraction; Diamond anvil cell; Differential stress; Hardness; *in situ* High-pressure; Non-hydrostatic compression; Radial diffraction; Rhenium diboride; Superhard materials; Tungsten tetraboride; X-ray diffraction.

I. INTRODUCTION

Superhard materials are of importance in a variety of high-speed cutting tool applications such as lathing, milling, drilling and sawing. As a new family of superhard solids, transition metal borides have demonstrated interesting properties including facile synthesis at ambient pressure, high electrical conductivity, and excellent elastic moduli.[1-4] Recently, the focus of research in the field of superhard materials has been redirected toward the inexpensive borides, a prime example of which is tungsten tetraboride (WB_4).[5] With a Vickers microindentation hardness of 43.3 ± 2.9 GPa, under an applied load of 0.49 N, WB_4 has drawn increasing research to understand its very high hardness.[5-8]

In general, hardness is calculated from the size of the indentation mark left by the tip of an indenter. In turn, the size of an indent depends on the material's response to compression, and its capacity to withstand deformations in the directions different from that of the applied load.[9] Since examining those bond deformations and stress states of materials is a nearly impossible task, high-pressure X-ray diffraction can be used as a versatile tool to characterize a material's response under compression, and therefore, to study its behavior under indentation.[3, 7, 10] Based on this idea, Gu *et al.* performed X-ray powder diffraction up to pressures of 34 GPa at ambient temperature on WB_4, and reported a bulk modulus of 304 ±10 GPa by fitting the second-order Birch-Murnaghan equation of state (EOS).[11] Liu *et al*. studied the high-pressure behavior of WB_4 up to 50.8 GPa with silicone oil as the pressure media. The authors obtained values ranging from 256 to 342 GPa, depending on the EOS and the pressure range.[12] In our recent work, the bond stiffness of WB_4 and its response upon hydrostatic compression were measured using *in situ* high-pressure X-ray diffraction.[7] We obtained a zero-pressure bulk modulus of 324 ± 3 GPa using the second-order Birch-Murnaghan equation of state. Moreover, at a hydrostatic pressure

of 42 GPa, we found that WB_4 underwent a reversible second-order phase transition that was attributed to its rigid structure. The broad variation in reported values is likely due in part to the rather subtle nature of this 2nd order phase transition. Because this phase transition was not recognized by many earlier workers studying WB_4,[12] equations of state were fit across both phases in some cases, producing wildly varying bulk modulus values, depending on the pressure range used. We note that this transition, was not observed in ReB_2, another member of the family of superhard transition metal borides that possesses a hardness close to WB_4, when compressed to similar pressures. We hypothesize that this is because the structure of ReB_2 is less constrained than WB_4. In all of these previous experiments, however, the material was compressed under hydrostatic stress condition in the diamond anvil cell (DAC), which does not fully represent the anisotropic stress condition that occur under the indenter's tip.

Radial X-ray diffraction, which determines the differential stress that each lattice plane can support, is an emerging DAC technique that permits data collection from materials under non-hydrostatic stress conditions.[13-15] In this method, the sample is compressed uniaxially and the X-ray beam is directed onto the sample through an X-ray transparent gasket (Figure 1).[16] Diffraction data are then collected from the lattice planes at all angles with respect to the maximum and minimum stress directions. This technique enables one to measure the elastically-supported differential stress, which provides a lower-bound estimate of the material's yield strength – the stress at which the material begins to deform plastically.[17-19] Since the yield strength is directly related to the material's hardness, the measurements of differential stress can greatly improve our understanding of the materials' macroscopic mechanical properties. In addition, some information can be gathered about the anisotropic nature of the lattice strain under deformation.

Using the radial diffraction technique, strong transition metal borides have been demonstrated to withstand high differential stresses.[3, 10, 20] Dong *et al.* investigated nanocrystalline tungsten monoboride (WB) under non-hydrostatic compression in a DAC and measured a differential stress of ~14 GPa at the highest pressure of 60.4 GPa.[20] Chung *et al.* found that the differential stress of superhard ReB_2 depends on the lattice planes, with values ranging from 6.4 to 12.9 GPa at a pressure of 14 GPa.[3] The lattice-dependent differential stress was also seen in hard OsB_2, with an average differential stress of 11 GPa at 27.5 GPa.[10] Most recently, Xiong *et al.* studied the equation of state of WB_4, synthesized using a hot press, under non-hydrostatic condition up to 85.8 GPa.[21] Unfortunately, the stress states and lattice anisotropy of the material were not explored in that study. In addition, the authors observed a smooth compression curve under equivalent hydrostatic conditions and found that the *a*-axis was more incompressible than the *c*-axis. These results, however, contrast with the observed second-order phase transition and the more compressible *a*-axis during hydrostatic compression reported in our previous hydrostatic study.[7]

Hence, our current study aims to examine the high-pressure behavior of WB_4 under non-hydrostatic conditions, with a goal of 1) clarifying the lattice strain including anisotropy, and 2) resolving the conflicts in the compression pathway and the directional compressibility of this material. We have undertaken a complete experimental study of the deformation behavior of WB_4 under uniaxial stress conditions using synchrotron-based angle-dispersive radial X-ray diffraction in the diamond anvil cell up to 48.5 GPa. A similar set of experiments were performed on ReB_2 up to 51.4 GPa, which allows us to compare and contrast the behavior of these two interesting superhard transition metal borides (both with space group $P6_3/mmc$).

II. EXPERIMENTAL PROCEDURE

Radial X-ray diffraction measurements of WB_4 and ReB_2 in a diamond anvil cell were performed in an angle-dispersive geometry at the beamline 12.2.2 of the Advanced Light Source (ALS, Lawrence Berkeley National Lab). Polycrystalline WB_4 and ReB_2 ingots, synthesized by arc melting from pure elements, were ground to fine powders with a grain size of <20 μm. Diamonds with a 350-μm tip diameter were chosen. To allow diffraction in a direction orthogonal to the compression axis, ~70-μm hole was drilled in a confining gasket made of amorphous boron and epoxy.[16] This 50-μm thick and 400-μm diameter gasket was then embedded in a small rectangular Kapton sheet. Two pre-compressed WB_4 platelets of 40-μm diameter were deposited at the bottom of the gasket hole. A platinum (Pt) flake, 30-μm in size, was then added into the gasket hole as an internal pressure standard. No pressure-transmitting medium was used in order to create a non-hydrostatic environment in the DAC. We loaded the ReB_2 sample using the same method and geometry.

To collect diffraction patterns, a monochromatic X-ray beam with a wavelength of 0.4959 Å, and size of 20 × 20 μm, was collimated on samples perpendicular to the loading axis. The distance and orientation of the image plate detector were calibrated with powder LaB_6. The measured pressure ranges were 0-48.5 and 0-51.4 GPa for WB_4 and ReB_2, respectively, with an increment of 3-8 GPa. We estimated the equivalent hydrostatic pressures from the equation of state of Pt after correcting the data for the effect of non-hydrostatic stress.[22]

To study the variations in the position of diffraction peaks with the image plate azimuthal angle η, two-dimensional diffraction patterns were "unrolled" into cake diffraction patterns with FIT2D.[23, 24] The cake pattern is a graph of the azimuthal angle η (between 0° and 360°) as a

function of diffraction angles 2θ (in degree). Here the standard diffraction rings become diffraction lines that look like layers on a cake. Importantly, the sinusoidal variation with azimuthal angle η in the cake diffraction patterns demonstrates the lattice deformation that result from the non-hydrostatic conditions. Generated cake patterns were then imported as images into Igor Pro (WaveMetrics, Inc.) where diffraction lines were read individually. Six diffraction peaks for WB_4 (101, 002, 110, 201, 112, 103) and seven peaks of ReB_2 (002, 100, 101, 102, 004, 103, 110) were resolved and used in the analysis. The angle between the diffracting plane normal and the loading axis, φ, was calculated from $\cos\varphi = \cos\theta \cdot \cos\eta$, where θ is the diffraction angle.[25]

III. METHODS

According to lattice strain theory,[17-19] the state of stress in the sample under uniaxial compression can be described as

$$\sigma = \begin{bmatrix} \sigma_1 & 0 & 0 \\ 0 & \sigma_1 & 0 \\ 0 & 0 & \sigma_3 \end{bmatrix} = \begin{bmatrix} \sigma_P & 0 & 0 \\ 0 & \sigma_P & 0 \\ 0 & 0 & \sigma_P \end{bmatrix} + \begin{bmatrix} -t/3 & 0 & 0 \\ 0 & -t/3 & 0 \\ 0 & 0 & 2t/3 \end{bmatrix}, \quad (1)$$

where σ_1 and σ_3 are the radial and axial principal stresses, respectively; σ_P, is the mean of the principal stress or hydrostatic stress component. The difference between σ_1 and σ_3 is the uniaxial stress component *t,*

$$t = \sigma_3 - \sigma_1 \leq 2\tau = \sigma_y, \quad (2)$$

where τ is the shear strength and σ_y is the yield strength of the material. The equality in relation (2) holds for a von Mises yield condition and a measurement of the elastically-supported differential stress, *t*, provides a lower-bound estimate on the material's yield strength, σ_y.

The equation for the *d* spacings measured by X-ray diffraction is given by the following relation:

$$d_m(hkl) = d_p(hkl)[1 + (1 - 3\cos^2\varphi)Q(hkl)], \quad (3)$$

where $d_m(hkl)$ is the measured *d* spacing and $d_p(hkl)$ is the *d* spacing due to the hydrostatic component of the stress, and $Q(hkl)$ is given by

$$Q(hkl) = \frac{t}{3}\left[\frac{\alpha}{2G_R(hkl)} + \frac{1-\alpha}{2G_V}\right]. \quad (4)$$

t is the applied differential stress, α is a value between 0 and 1 that describes the continuity behavior of the polycrystalline materials, and $G_R(hkl)$ and G_V are the shear moduli of the aggregate under the Reuss (isostress) and Voigt (isostrain) approximations, respectively. The shear moduli are functions of the single crystal elastic compliances – five independent ones for hexagonal WB_4 and ReB_2. According to Eqn. (3), the *d* spacing value at $(1 - 3\cos^2\varphi) = 0$, i.e. φ = 54.7°, corresponds to the hydrostatic component of the stress. Angles φ = 0° and 90° correspond to the normal of the diffraction lattice plane being parallel and perpendicular to the applied load, respectively. The measured *d* spacing value in these two orientations is maximum and minimum, respectively.

Most high-pressure experiments assume isostress conditions; thus the uniaxial stress components in the different diffraction planes are taken as identical.[26] In anisotropic materials

like WB_4 and ReB_2, however, the assumption of isostress conditions may not be valid. Hence, the differential stress t has to be calculated for each different diffraction planes. According to Eq. (4), the differential stress supported by a set of lattice planes (*hkl*) can be estimated using the relation[26, 27]

$$t(hkl) = 6\, G(hkl)\, Q(hkl). \quad (5)$$

$G(hkl)$ is the shear modulus of lattice planes (*hkl*). The ratio of the differential stress to shear modulus $t(hkl)/G(hkl)$ can be a useful parameter in describing contributions of both plastic and elastic deformation.[26, 28] $t(hkl)/G(hkl)$ is readily determined from the ratio of the slope to the intercept of the d_m (*hkl*) vs $1\text{-}3\cos^2\varphi$ graphs. If the differential stress has reached its limiting value of yield strength at high pressures, $6Q(hkl) = t(hkl)/G(hkl)$ will reflect the ratio of yield strength of lattice plane (*hkl*) to shear modulus.

IV. RESULTS

Figure 2 shows representative diffraction patterns of WB_4 taken at $\varphi = 0°$, 55° and 90° at pressures of 5.5 and 45.4 GPa. Each diffraction pattern is an integration over 5° intervals. All patterns are indexed to the hexagonal WB_4 phase ($P6_3/mmc$),[29] and there are no signs of phase transformations. As φ increases from 0° to 90°, diffraction peaks shift to smaller 2θ in both sets of spectra. This indicates that the lattice planes of WB_4 are subject to less strain as the diffraction plane's normal approaches the minimum stress axis.

Figure 3 shows the variation of the d spacing as a function of $1\text{-}3\cos^2\varphi$ for the first four observed reflections of WB_4 at the highest pressure. The slope of each line provides information of the differential stress supported by each lattice plane and the shear modulus. As expected from the theory (Eqn. 3), the measured d spacings vary linearly with $1\text{-}3\cos^2\varphi$. The compression

curves of WB_4 as a function of pressure at $\varphi = 0°$ (up triangles), 54.7°(circles) and 90°(down triangles) are shown in Fig. 4a. The unit cell volumes observed at different pressures are fitted to the third-order Birch-Murnaghan EOS. The bulk modulus K_0 corresponding to the hydrostatic compression curve ($\varphi = 54.7°$) in the entire pressure range is 309 ± 5 GPa with $K_0' = 2.4 \pm 0.3$. The hydrostatic compression data can thus be obtained from highly non-hydrostatic data by choosing proper angle between the stress axis and the diffraction vector.

To examine the directional compressibility of WB_4 under non-hydrostatic conditions, we plot compression curves for the lattice parameters, *a* and *c* (Fig. 4b). Both lattice constants decrease continuously with increasing pressure before 15 GPa, and the *c*-axis is less compressible than the *a*-axis. At 15 GPa, a change in the slope of the decrease for the *c*-axis was seen in the minimum stress direction $\varphi = 90°$, indicating a structural change. This anomalous drop in the *c*-axis, however, is less dramatic at $\varphi = 54.7°$, and is not visible at $\varphi = 0°$. In contrast, the *a*-axis does not show any changes in slope at all stress directions.

To verify this abrupt change, we cross-compare the high-pressure behaviors of WB_4 with ReB_2, one of the hardest transition metal borides known to date. We examined the *c*/*a* ratio of WB_4 and ReB_2 normalized to each other at various stress directions ($\varphi = 0°$, 54.7° and 90°) (Fig. 5). Because of the non-hydrostatic stress state in the high-pressure cell, in all cases, we paired orthogonal *c*-axis and *a*-axis data. In other words, for $\varphi = 0°$, we used high stress *c*-axis data, and ratioed that to low stress *a*-axis data because a grain in the DAC with the *c*-axis oriented along the high stress direction must have its *a*-axis oriented along the low stress direction. Up to 15 GPa, the *c*/*a* ratio shows a linear increase in both materials at $\varphi = 90°$(*c*-axis)/0°(*a*-axis). For ReB_2, this linear increase continues to pressures in excess of 50 GPa. In contrast, there is a

discontinuous change in slope for the c/a ratio of WB_4 for pressures above 15 GPa. This discontinuity is also observed at $\varphi = 54.7°$ (Fig. 5a). We note that while the slope of the data shown in Figure 5 is sensitive to our choice to use orthogonal c- and a-axis data, because there are no discontinuous changes in the a-axis data at any φ, the presence of a discontinuous slope changes in the c/a ratio is robust across all choices of a-axis data. At $\varphi = 0°$(c-axis)/90°(a-axis), the c/a ratio of WB_4 shows no discontinuous changes, but the value decreases across the entire pressure range (Fig. 5a). This results is in contrast with the steady increase in $\varphi = 0°$(c-axis)/90°(a-axis) c/a ratio in ReB_2 over the entire pressure range (Fig. 5b).

Because of this structural change in WB_4, we only used data up to 15 GPa to fit the volume-pressure data. Using the third-order Birch-Murnaghan EOS, the zero-pressure bulk modulus K_0 obtained at $\varphi = 54.7°$ is 306 ± 19 GPa with $K_0' = 3.3 \pm 2.8$. The relative large errors are due to the limited data (up to 15 GPa) used in the fitting. This value is within error of the bulk modulus of 326 ± 3 GPa measured from quasi-hydrostatic compression using the second order Birch-Murnaghan EOS.[7] Because of the value of K_0' can have a significant impact on the resultant K_0 value, however, we also recalculated a "matched" K_0 value from the quasi-hydrostatic data using a fixed $K_0' = 3.3$ to match the data presented here. That value, 334 ± 19 GPa, is slightly higher than the previously reported value, but is still within experimental error of the $\varphi = 54.7°$ bulk modulus reported here. As an exercise, we also calculated bulk moduli using the second-order Birch-Murnaghan EOS from data obtained at the maximum stress direction $\varphi = 0°$ and minimum stress direction $\varphi = 90°$. The values obtained were 188 ± 1 GPa and 443 ± 8 GPa, respectively, numbers that vary by more than a factor of 2. We present these values not to indicate that they are meaningful bulk moduli under non-hydrostatic conditions, but instead to illustrate the profound effect that non-hydrostaticity in a diamond cell can have on the calculated

bulk modulus. The errors can be particularly large when investigating the equation of states of superhard materials such as WB_4.

To obtain the total differential stress that a material can stand without yielding, one needs to take into account its shear modulus. Unfortunately, neither shear modulus nor elastic moduli has been experimentally measured for WB_4. Therefore, we looked at the ratio of differential stress *t(hkl)* to shear modulus *G(hkl)*. The *t(hkl)*/*G(hkl)* ratio is a reflection of the elastically-supported differential strain in the lattice planes under an imposed differential stress.[10] Figure 6a shows the *t(hkl)*/*G(hkl)* ratio of representative sets of planes as a function of pressure for WB_4 and ReB_2. The *t(hkl)*/*G(hkl)* increases with pressures for all planes and it saturates at 4-6.2% and 1.7-2.9% for WB_4 and ReB_2, respectively. This indicates that WB_4 can either support a higher differential stress than ReB_2, or possess a lower shear modulus.

To estimate the differential stress supported by WB_4 and compare it to that of ReB_2, we used a calculated zero-pressure shear modulus (G_0) of 249 GPa for WB_4[7] and the measured value of 273 GPa for ReB_2.[30] The shear modulus at elevated pressures were approximated by extrapolating the zero-pressure values using the pressure derivative dG/dP of 1.5, which is typical for ceramics,[31] and is also used for cermet and intermetallic materials, such as WB[20] and TiB_2.[26] Figure 6b shows the differential stress *t(hkl)* of WB_4 and ReB_2 as a function of pressure for studied lattice planes. The differential stress in all lattice directions increases almost linearly until a plateau value is reached. WB_4 and ReB_2 yield at pressures of 30-40 GPa and ~20 GPa, respectively. When the average value of t at plateau – t(average) – is approximated by taking the average plateau value of t(002), t(101), and t(110), a value of 15.8 and 7.2 GPa is deduced for WB_4 and ReB_2 at the highest measured pressure, respectively. We note that the differential stress supported by ReB_2 is lower than that reported by Chung *et al.,*[3] which could be due to an

underestimation of the pressure in the DAC in their study. The differential stress of WB_4 is slightly lower than that measured for nanocrystalline γ-Si_3N_4 (~18.5 GPa),[32] and significantly lower than the value obtained for microcrystalline B_6O (~24.5 GPa) in the similar pressure range.[28] Given that the measured high-load Vickers hardness of WB_4, 28.1 GPa, is also lower than that of γ-Si_3N_4 (35-43 GPa)[33-35] and B_6O (45 GPa),[36] the maximum differential stress values obtained here appear reasonable.

V. DISCUSSION

The abrupt change in the *c*/*a* ratio of WB_4 under non-hydrostatic compression agrees with our recent observation under hydrostatic compression of a second-order structural phase transition.[7] When WB_4 was compressed hydrostatically, however, the change occurred at a much higher pressure of 42 GPa compared to a pressure of 15 GPa under non-hydrostatic compression. Similar to the data obtain under hydrostatic compression, the WB_4 diffraction profiles remain the same during the entire non-hydrostatic compression run with no evidence of peak splitting. Thus, it appears that the phase transition is still second order in nature. Because this transition pressure (15 GPa) appears far from the pressure when WB_4 begins to yield (30-40 GPa), the structural change is not likely to be caused by plastic flow; but instead probably results from changes in optimal bonding under pressure within the elastic regime. In ReB_2, however, a continuous increase of the *c*/*a* ratio was found in regardless of the compression conditions within the measured pressure range. In order to understand the structural changes in WB_4 and the lack of similar changes in ReB_2 under non-hydrostatic compression, and to relate them to the observations under hydrostatic compression, it is helpful to consider the crystal structures of these two phases (Fig. 7).

The crystal structure of ReB_2 is characterized by puckered six-fold boron rings that are intercalated by Re layers that have partial metallic bonding.[37] The Re atoms are arranged in a hexagonal close-packed layer with B atoms occupying all tetrahedral voids. X-ray absorption spectroscopic data showed the B layers become flatten with increasing hydrostatic pressure, indicating a reduced structural rigidity of ReB_2 structure.[38] Because the layers are not highly constraint in the *a*-*b* direction, continuous structural rearrangements upon non-hydrostatic compression results in smooth and continuous change in the *c*-axis up to the highest pressures measured (51.4 GPa).

The generally accepted structure of WB_4 consists of alternating hexagonal layers of boron and tungsten atoms with B-B dimers with their bonding axis running along the *c*-axis direction that bridge between the boron layers.[5-7, 29, 39-44] Recently, the stoichiometry and structure of the superhard WB_4 phase has been challenged by Cheng *et al*., and a defect containing WB_{3+x} phase was suggested as the correct crystal structure for superhard WB_4.[45, 46] Most recently, our group has unambiguously solved the structure of WB_4 by refinement of combined X-ray powder, X-ray single crystal, and neutron time-of-flight powder diffraction data.[47] Our analysis indicates that some W atom sites are only partially occupied, and when these sites are unoccupied, boron trimers sit on those lattice sites with the boron atoms distributed between the partially occupied W sites and the interstitial space between W planes If the location of the boron trimers is correlated between layers, pseudo-cuboctahedral cages oriented along the c-axis can form and these cages have the potential to produce mechanically robust linkages between boron layers.

Compared to the ReB_2 structure, this additional covalently bonded boron along the *c* direction, particularly as it appears in the form of a rigid boron cage, should make the WB_4 structure much less flexible than the ReB_2 structure. We hypothesize that because of the more

constrained bonding in WB_4, it is unlikely that the ambient-pressure WB_4 structure can accommodate high pressures without rearrangement.

One other trend that needs to be explained is the apparent lack of a phase transition for non-hydrostatic data collected with the *c*-axis oriented along the high stress direction. Under hydrostatic compression a discontinuous change in the *c/a* ratio is observed at 42 GPa. This same discontinuity is observed at 15 GPa for data collected with the *c*-axis along the low stress direction and the *a*-axis oriented along the high stress direction. Based on this trend, we would expect to see an even lower transition pressure for non-hydrostatic data collected with the *a*-axis along the low stress direction and the *c*-axis oriented along the high stress direction. If we assume the transition happens at a fixed strain under non-hydrostatic conditions, we would predict a transition pressure <5 GPa. Unfortunately, the point density in our data is too low to clearly identify a transition at pressures that low, but we assume that both the negative slope and the lack of a well-defined phase transition point for the data shown in Figure 5a, $\varphi = 0°$, result because the 2nd order phase transition in this configuration occurs at pressures too low for us to measure.

While the pressure-induced bond rearrangements observed here are not a cause of the high hardness of WB_4, it is likely that the comparatively high hardness in WB_4 arises from the same bonding constraints in the three-dimensional boron network that are responsible for the phase transition. As we know, hardness is determined by the strength and directionality of local interatomic bonding interactions.[48] In a covalent solid, such as WB_4, the chemical bonds are localized and it is expected that the compressibility (or the bulk moduli), which is the resistance to volume change, may be connected to the hardness. This assumption, however, is only valid when the forces are applied isotropically.[48] This is not the case in indentation measurements or

non-hydrostatic compression where both normal and shear stresses are to be considered. Because of this, the hardness of a crystal is the ability to resist both elastic and plastic deformation under hydrostatic compression as well as tensile load and shear. In WB_4, the three-dimensional rigid boron network, consisting of both boron layers in the *a*-*b* plane and boron cages linking those layers together, not only resists isotropic compression (high bulk modulus), but also helps maintain the structural integrity from shear deformation (high yield strength), resulting in the exceptionally high hardness of WB_4.

In addition to examining phase stability and average plateau value of the differential stress, it is interesting to explore the strength anisotropy in WB_4 and ReB_2 by examining the lattice-dependent differential stress (Fig. 6b). The (004) planes in ReB_2, which are orthogonal to the *c* axis, are parallel to the layers of Re and B, and support the least differential stress due to the ability of these layers to slip. The (110) planes, on the other hand, are perpendicular to these slip planes, and are able to support a considerably higher differential stress. These results are reinforced by DFT calculations showing that the (001) direction is the easiest location for stress release due to a tendency to crack between atomic layers of metal and boron upon cleavage.[49] Unlike ReB_2, however, the (002) planes in WB_4, which are again parallel to the W layers, support a higher differential stress than either the (101) or (110) plane. We hypothesize that the newly discovered boron cuboctahedral cages discussed above are responsible for this remarkable reversal in what are otherwise rather similar structures. Boron cages are established as stable bonding structures, and if such cages link the boron layers together, cracks between atomic layers of metal and boron would necessitate destruction of those cages, which is bound to be energetically unfavorable. As a result, the (002) planes now become the least favorable locations for stress release, and are able to withstand a substantial differential stress. It is interesting to

note that when examining only the (101) and (110) planes, that WB_4 and ReB_2 support very similar differential stresses. The differences in these two materials are only clear when the very low and very high *t* values for the ReB_2 (004) and WB_4 (002) planes are included as well, a result that makes much more sense in light of the newly reported crystal structure described above.

In a previous lattice strain analysis based on radial X-ray diffraction technique, it has been pointed out the strength anisotropy may indicate stress variations due to a preferred slip system.[50] In ReB_2, the (004) planes support the least differential stress among the studied planes, and are likely to be the slip planes. First-principle calculations have also shown that $(001)[1\bar{1}0]$ is found to be the weakest direction during the plastic flow, resulting in significant weakening in the puckered hexagonal boron layer that is normally responsible for the high structural strength of ReB_2.[51] By contrast, in WB_4, the (002) planes are able to support a large *t*. The corresponding slip system, basal slip, is hence unlikely to be the principal slip system compared to other slip systems occurring in hexagonal structures, such as prism and pyramidal slip. This has been seen in related calculated stress-strain relations of hexagonal WB_4 where the [001] direction supports the highest stress under tensile loading.[42]

VI. CONCLUSIONS

In summary, the stress states and compressive strength of superhard material WB_4 and ReB_2 were studied using X-ray radial diffraction experiment in the diamond anvil cell under non-hydrostatic compression up to 48.5 and 51.4 GPa, respectively. In contrast to ReB_2, we observed an abrupt *c/a* ratio change in WB_4 at 15 GPa due to structural rearrangements that likely arise from the rigid nature of the WB_4 network. Lattice dependent strength anisotropy was further investigated in WB_4 and ReB_2. We found that the (002) plane of WB_4 supported the largest

differential stress among studied planes because additional covalent boron bonding along the *c* direction significant prevented boron layers from shearing. The (004) plane in ReB_2, however, supports the least differential stress due to the ability of the layers to slip.

There were also significant differences in the magnitude of the limiting differential stress supported by WB_4 and ReB_2. WB_4 is able to sustain a maximum differential stress of 19.7 GPa at a confining pressure of 48.5 GPa, while ReB_2 supports a differential stress of 9.2 GPa within a similar pressure range. We hypothesize that it is the three-dimensional covalent boron bonding network in WB_4 that is responsible for its high hardness and high yield strength.

By examining the lattice behavior of superhard materials like WB_4 under non-hydrostatic compression at elevated pressures, we begin to understand the material's capacity to withstand deformations in a direction different from applied load. Although the stress states of a material under non-hydrostatic compression are not fully representations of the stress conditions than happen under the indenter's tip, they do significantly advance our understanding of the deformation behavior of the materials under non-hydrostatic conditions in a lattice specific manner. This should be useful in the future design of new superhard transition metal borides, particularly in assessing the correlation between structural, elastic, and mechanical properties.

ACKNOWLEDGMENTS

The authors thank A. T. Lech for the crystal structural analysis, B. Chen for preparing the boron epoxy gaskets, and M. T. Yeung, S. Raju, Z. Mao for experimental assistance. We also thank W. Kanitpanyacharoen, Professor H.-R. Wenk and Professor T. S. Duffy for equipment support. This work was funded by the National Science Foundation under grant DMR-0805357 (SHT and RBK). Portions of this work were performed at the Advanced Light Source (LBNL).

The Advanced Light Source is supported by the Director, Office of Science, Office of Basic Energy Sciences, of the U.S. Department of Energy under Contract No. DE-AC02-05CH11231. This research was partially supported by COMPRES, the Consortium for Materials Properties Research in Earth Sciences under NSF Cooperative Agreement EAR 11-57758.

REFERENCES

[1] J. B. Levine, S. H. Tolbert, and R. B. Kaner, Advanced Functional Materials **19**, 3519 (2009).

[2] R. Mohammadi and R. B. Kaner, in *Encyclopedia of Inorganic and Bioinorganic Chemistry*, edited by R. A. Scott (John Wiley: Chichester, 2012).

[3] H.-Y. Chung, M. B. Weinberger, J. B. Levine, A. Kavner, J.-M. Yang, S. H. Tolbert, and R. B. Kaner, Science **316**, 436 (2007).

[4] J. B. Levine, S. L. Nguyen, H. I. Rasool, J. A. Wright, S. E. Brown, and R. B. Kaner, Journal of the American Chemical Society **130**, 16953 (2008).

[5] R. Mohammadi, A. T. Lech, M. Xie, B. E. Weaver, M. T. Yeung, S. H. Tolbert, and R. B. Kaner, Proceedings of the National Academy of Sciences of the United States of America **108**, 10958 (2011).

[6] R. Mohammadi, M. Xie, A. T. Lech, C. L. Turner, A. Kavner, S. H. Tolbert, and R. B. Kaner, Journal of the American Chemical Society **134**, 20660 (2012).

[7] M. Xie, R. Mohammadi, Z. Mao, M. M. Armentrout, A. Kavner, R. B. Kaner, and S. H. Tolbert, Physical Review B **85** (2012).

[8] R. F. Zhang, D. Legut, Z. J. Lin, Y. S. Zhao, H. K. Mao, and S. Veprek, Physical Review Letters **108** (2012).

[9] J. Haines, J. M. Leger, and G. Bocquillon, Annual Review of Materials Research **31**, 1 (2001).

[10] A. Kavner, M. B. Weinberger, A. Shahar, R. W. Cumberland, J. B. Levine, R. B. Kaner, and S. H. Tolbert, Journal of Applied Physics **112** (2012).

[11] Q. Gu, G. Krauss, and W. Steurer, Advanced Materials **20**, 3620 (2008).

[12] C. Liu, F. Peng, N. Tan, J. Liu, F. Li, J. Qin, J. Wang, Q. Wang, and D. He, High Pressure Research **31**, 275 (2011).

[13] H. K. Mao, J. F. Shu, G. Y. Shen, R. J. Hemley, B. S. Li, and A. K. Singh, Nature **396**, 741 (1998).

[14] S. Merkel, Journal of Physics-Condensed Matter **18**, S949 (2006).

[15] T. S. Duffy, AIP Conference Proceedings **955**, 639 (2007).

[16] S. Merkel and T. Yagi, Review of Scientific Instruments **76** (2005).

[17] A. K. Singh, C. Balasingh, H. K. Mao, R. J. Hemley, and J. F. Shu, Journal of Applied Physics **83**, 7567 (1998).

[18] A. K. Singh, Journal of Physics and Chemistry of Solids **65**, 1589 (2004).

[19] A. K. Singh, Journal of Applied Physics **73**, 4278 (1993).

[20] H. Dong, S. M. Dorfman, Y. Chen, H. Wang, J. Wang, J. Qin, D. He, and T. S. Duffy, Journal of Applied Physics **111** (2012).

[21] L. Xiong, J. Liu, L. Bai, Y. Li, C. Lin, D. He, F. Peng, and J.-F. Lin, Journal of Applied Physics **113** (2013).

[22] Y. W. Fei, A. Ricolleau, M. Frank, K. Mibe, G. Y. Shen, and V. Prakapenka, Proceedings of the National Academy of Sciences of the United States of America **104**, 9182 (2007).

[23] A. P. Hammersley, S. O. Svensson, M. Hanfland, A. N. Fitch, and D. Hausermann, High Pressure Research **14**, 235 (1996).

[24] See Supplemental Material at [*URL will be inserted by publisher*] for integrated cake diffraction patterns of WB_4.

[25] S. Merkel, H. R. Wenk, J. F. Shu, G. Y. Shen, P. Gillet, H. K. Mao, and R. J. Hemley, Journal of Geophysical Research-Solid Earth **107** (2002).

[26] G. M. Amulele, M. H. Manghnani, and M. Somayazulu, Journal of Applied Physics **99** (2006).

[27] Y. B. Wang, T. Uchida, R. Von Dreele, M. L. Rivers, N. Nishiyama, K. Funakoshi, A. Nozawa, and H. Kaneko, Journal of Applied Crystallography **37**, 947 (2004).

[28] D. W. He, S. R. Shieh, and T. S. Duffy, Physical Review B **70** (2004).

[29] P. A. Romans and M. P. Krug, Acta Crystallographica **20**, 313 (1966).

[30] J. B. Levine, J. B. Betts, J. D. Garrett, S. Q. Guo, J. T. Eng, A. Migliori, and R. B. Kaner, Acta Materialia **58**, 1530 (2010).

[31] D. G. Isaak, *Handbook of Elastic Properties of Solids, Liquids, and Gases* (Academic Press, San Diego, CA, 2001).

[32] B. Kiefer, S. R. Shieh, T. S. Duffy, and T. Sekine, Physical Review B **72** (2005).

[33] J. Z. Jiang, F. Kragh, D. J. Frost, K. Stahl, and H. Lindelov, Journal of Physics-Condensed Matter **13**, L515 (2001).

[34] I. Tanaka, F. Oba, T. Sekine, E. Ito, A. Kubo, K. Tatsumi, H. Adachi, and T. Yamamoto, Journal of Materials Research **17**, 731 (2002).

[35] A. Zerr, G. Miehe, G. Serghiou, M. Schwarz, E. Kroke, R. Riedel, H. Fuess, P. Kroll, and R. Boehler, Nature **400**, 340 (1999).

[36] D. W. He, Y. S. Zhao, L. Daemen, J. Qian, T. D. Shen, and T. W. Zerda, Applied Physics Letters **81**, 643 (2002).

[37] M. Frotscher, M. Hoelzel, and B. Albert, Zeitschrift Fur Anorganische Und Allgemeine Chemie **636**, 1783 (2010).

[38] J. Pellicer-Porres, A. Segura, A. Munoz, A. Polian, and A. Congeduti, Journal of Physics-Condensed Matter **22** (2010).

[39] H. Nowotny, H. Haschke, and Benesovs.F, Monatshefte Fur Chemie **98**, 547 (1967).

[40] Y. Liang, Z. Fu, X. Yuan, S. Wang, Z. Zhong, and W. Zhang, Epl **98** (2012).

[41] Q. Li, D. Zhou, W. Zheng, Y. Ma, and C. Chen, Physical Review Letters **110** (2013).

[42] H. Gou, Z. Li, L.-M. Wang, J. Lian, and Y. Wang, Aip Advances **2** (2012).

[43] M. Zhang, H. Yan, Q. Wei, and H. Wang, Computational Materials Science **68**, 371 (2013).

[44] M. Zhang, H. Wang, H. Wang, T. Cui, and Y. Ma, The Journal of Physical Chemistry C **114**, 6722 (2010).

[45] X. Cheng, W. Zhang, X.-Q. Chen, H. Niu, P. Liu, K. Du, G. Liu, D. Li, H.-M. Cheng, H. Ye, and Y. Li, Applied Physics Letters **103** (2013).

[46] X. Y. Cheng, X. Q. Chen, D. Z. Li, and Y. Y. Li, Acta Crystallographica Section C-Crystal Structure Communications **70**, 85 (2014).

[47] A. T. Lech, R. Mohammadi, C. L. Turner, S. H. Tolbert, and R. B. Kaner, (2014).

[48] J. S. Tse, Journal of Superhard Materials **32**, 177 (2010).

[49] P. Lazar, X.-Q. Chen, and R. Podloucky, Physical Review B **80** (2009).

[50] W. L. Mao, V. V. Struzhkin, A. Q. R. Baron, S. Tsutsui, C. E. Tommaseo, H.-R. Wenk, M. Y. Hu, P. Chow, W. Sturhahn, J. Shu, R. J. Hemley, D. L. Heinz, and H.-K. Mao, Journal of Geophysical Research-Solid Earth **113** (2008).

[51] C. Zang, H. Sun, J. S. Tse, and C. Chen, Physical Review B **86** (2012).

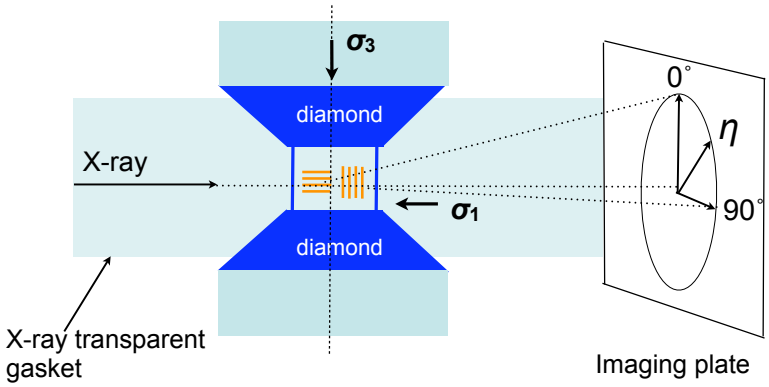

Figure 1. Schematic of the experiment. The polycrystalline sample is confined under non-hydrostatic stress conditions between the two diamond anvils. σ_1 and σ_3 are the radial and axial stress components, respectively. A monochromatic X-ray beam is sent through the gasket with the direction of the incoming beam orthogonal to the diamond axis and the data collected on an imaging plate normal to the incoming beam. The position of the diffraction lines and intensity of diffraction are analyzed as a function of the azimuthal angle η.

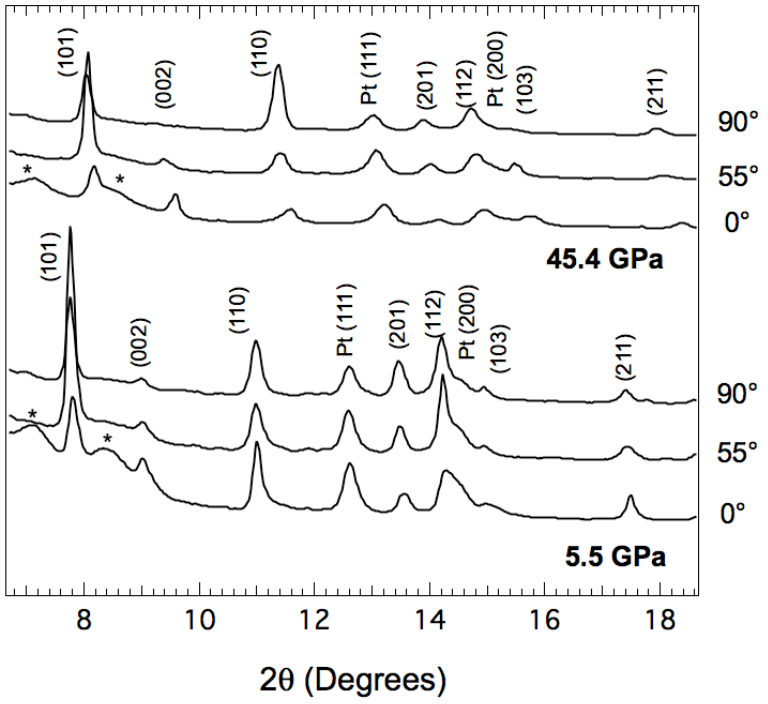

Figure 2. Representative line scans extracted from 2-dimensional diffraction patterns at 5.5 and 45.4 GPa for $\varphi = 0°$, 55°, and 90° obtained with integrations over 5° intervals. Diffraction peaks are labeled with miller indices for WB_4 and Pt. The asterisks indicate diffraction from boron-epoxy gasket.

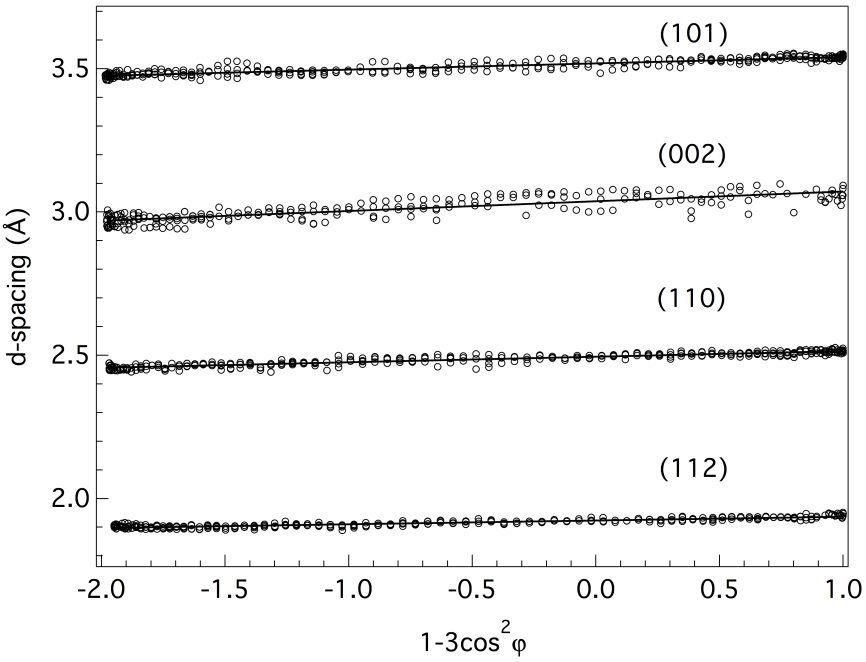

Figure 3. Dependence of measured *d* spacings on 1-3cos$^2\varphi$ for (101), (002), (110) and (201) diffraction lines of WB_4 at the highest pressure of 48.5 GPa. The solid lines are linear fit to the data.

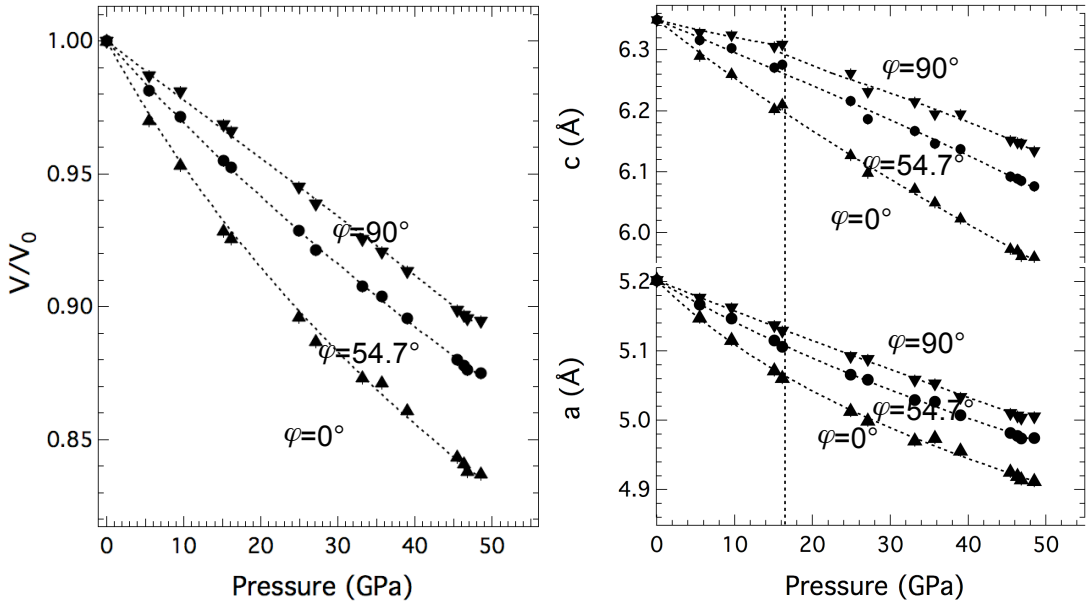

Figure 4. Evolution of the unit cell volume (a) and the lattice parameters (b) as a function of pressure in WB_4 under non-hydrostatic compression. The dashed lines fit to the Birch-Murnaghan EOS. The error bars when not shown are smaller than the symbol. At ~15 GPa during non-hydrostatic compression, the slope of the *c*-lattice constant presents a discontinuity at 54.7° and 90°. The *a*-lattice constant does not exhibit this slope discontinuity.

ab

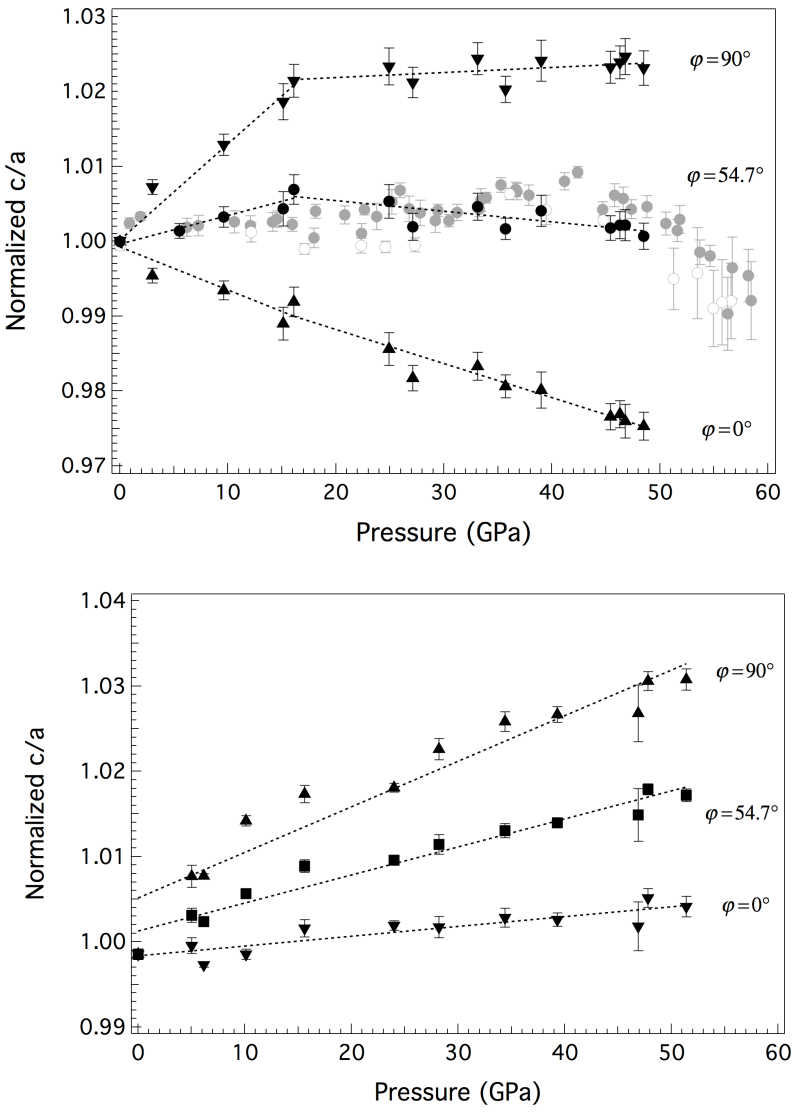

Figure 5. The normalized *c*/*a* ratio evolution as a function of pressure in WB_4 (a) and ReB_2 (b) under hydrostatic (grey) and non-hydrostatic (black) compression. Grey closed and open circles in (a) are values from *in-situ* X-ray diffraction under hydrostatic compression and decompression, respectively. Black symbols correspond to data collected under non-hydrostatic conditions and the collection angle is specified on the graph. In all cases, the indicated collection angle corresponds to the *c*-axis data, and is paired with orthogonal *a*-axis data (i.e. 0º *c*/90º *a*, 54.7º *c*/54.7º *a*, 90º *c*/0º *a*). Lines are linear fits to the data and are intended only to guide the eye. The error bars when not shown are smaller than the symbols.

a
b

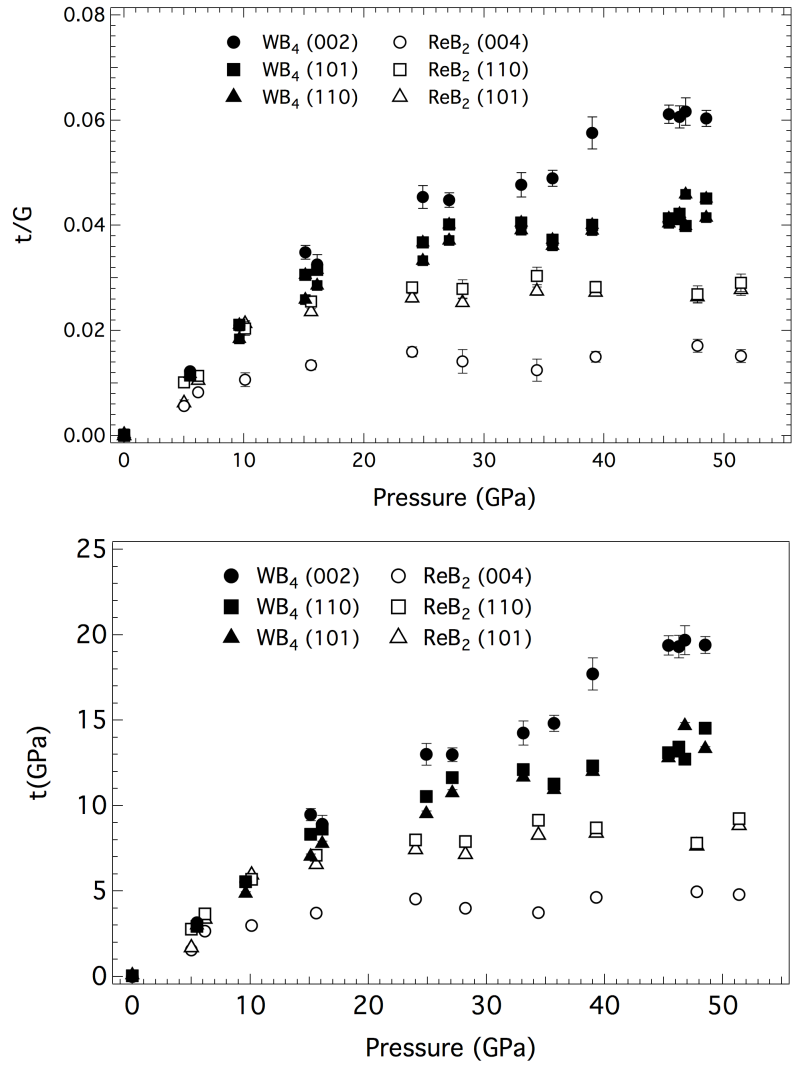

Figure 6. Differential strain (*t(hkl)*/*G*) (a) and differential stress *t(hkl)* (b) as a function of pressure for three lattice planes in WB_4 and ReB_2. Both WB_4 and ReB_2 demonstrated a strain/strength anisotropy. In WB_4, the (002) planes are able to support the highest differential stress of 19.7 GPa at the 50 GPa. By contrast, in ReB_2, the (004) planes support the least amount of differential stress.